Supporting Information for "Multiple Observations of the Prompt Elastogravity Signals Heralding Direct Seismic Waves"

Martin Vallée[1] and Kévin Juhel[1,2]

[1]Institut de Physique du Globe de Paris, Sorbonne Paris Cité, Université Paris Diderot, CNRS, France

[2]AstroParticule et Cosmologie, Paris, France

Contents of this file

1. Text S1 to S2
2. Figures S1 to S6

Introduction

In these supplementary materials, Section S1 and associated Fig. S1 tackle the numerical challenge of computing surface maps of the gravity-induced elastic effect with low computational costs. Section S2 and associated Figs. S2 to S5 then demonstrate the importance of computing both the direct gravity effect and the gravity-induced elastic effect to get accurate estimations of the overall prompt elastogravity signals (PEGS), and thus provide guidance for the search of new PEGS observations. Figure S6 finally shows,

---

Corresponding author: M. Vallée, Institut de Physique du Globe de Paris, 1 rue Jussieu 75005 Paris (vallee@ipgp.fr).

in the case of the Gulf of Alaska earthquake, that PEGS are still unambiguously detected even without optimizing the stations to be considered in the optimal stack (as done in Figure 7). It also illustrates the inefficiency of a simple stack approach compared to the optimal stack strategy, when an excessive number of stations - potentially of low quality - is included.

S1. Surface map simulation of the gravity-induced elastic effect.

Prompt elastogravity signals (PEGS) are modeled as the difference between a direct gravity effect ($\Delta\mathbf{g}$) and a gravity-induced elastic effect ($\ddot{\mathbf{u}}^{\mathbf{P}}$) (Vallée et al., 2017). To model the PEGS and get the surface maps shown in the main manuscript, we use the normal-mode formalism described in Juhel et al. (2018).

The normal-mode formalism enables the computation of the direct gravity effect $\Delta\mathbf{g}$ in a straightforward mode summation. However, the normal-mode computation of the induced effect $\ddot{\mathbf{u}}^{\mathbf{P}}$ requires a two-step approach, thus, a larger computation time. Indeed, it requires first to compute the gravity perturbation $\Delta\mathbf{g_k}$ induced by the earthquake in the volume surrounding the location ($\boldsymbol{r}$) where we want to compute $\ddot{\mathbf{u}}^{\mathbf{P}}$. This volume is roughly a half-ball grid of points ($\boldsymbol{r_k}$) centered around ($\boldsymbol{r}$), whose radius is the epicentral distance. Then, the secondary elastic waves induced by the body forces $\rho\Delta\mathbf{g_k}$ are summed at the considered location ($\boldsymbol{r}$) into the induced elastic effect $\ddot{\mathbf{u}}^{\mathbf{P}}$.

Juhel et al. (2018) used a different grid of points ($\boldsymbol{r_k}$) to compute $\ddot{\mathbf{u}}^{\mathbf{P}}$ at each of the considered station locations. For nearby stations, such approach leads to an overlap of the ($\boldsymbol{r_k}$) grids, meaning that the body forces $\rho\Delta\mathbf{g_k}$ may be inefficiently computed several times for the same location. In this study, as we want to compute $\ddot{\mathbf{u}}^{\mathbf{P}}$ every 40 kilometers from

0° to 20° away from the epicenter location (more than 12 000 locations), this inefficiency becomes critical.

In order to make the numerical approach more tractable, we first define a single, large, regular 3D grid centered at the epicenter location, with grid points every 40 kilometers in latitude and longitude, and sampling each layer of the PREM model. For each point of this grid, the body forces $\rho\Delta\mathbf{g_k}$ induced by the four earthquakes considered in Section 2 are computed. The section of this 3D body forces grid at the Earth's surface is represented in Fig. S1, with the union of all dots.

On the other hand, we compute Green's functions in a single half-ball grid, relating each of the half-ball grid points - excited with an impulsive 3D force - to the central point of the grid. The radius of the half-ball is set to 30°.

From these two large grids of body forces and Green's functions, the induced elastic effect at the 12 000 locations inside the black lines of Fig. S1 can be computed. Two of these locations are represented by a yellow square in Fig. S1. For a given location, we use the following processing steps:

(a) we locate the central point of the half-ball Green's functions grid at this specific location,

(b) we select the points of the half-ball whose P-wave travel time to the central point is lower than the P travel time from the epicenter to the central point, as illustrated in Fig. S1 with the blue and green dots,

(c) we convolve the Green's functions thus selected with the corresponding body forces of the 3D $\rho\Delta\mathbf{g_k}$ grid,

(d) the overall sum of the convolutions is the induced effect at the specific location.

To get the overall map, we move the half-ball grid central point to each of the 12 000 point locations and repeat the processing steps.

S2. PEGS decomposition into their direct and induced effects.

In order to assess the importance of rupture depth and focal mechanism on PEGS amplitude, we consider in Section 2 of the main manuscript four different mechanisms: a shallow strike-slip, a deep dip-slip and two shallow subduction megathrust earthquakes (dip = 10° and 20°). The vertical PEGS amplitudes at P-wave arrival time for all four mechanisms are decomposed into their direct ($\Delta\mathbf{g}$) and induced elastic ($\ddot{\mathbf{u}}^{\mathbf{P}}$) effects in Figs. S2 to S5. Such decomposition illustrates the importance of modeling the two effects to get an accurate estimation of the overall expected PEGS.

Indeed, for the shallow strike-slip earthquake, although the radiation patterns of the direct effect and overall PEGS are similar, the induced effect considerably lowers the amplitude of the sole direct effect. For the deep dip-slip earthquake, the induced effect even over-compensates the direct effect amplitudes at P-wave arrival time. Furthermore, the epicentral distance at which the sign of the perturbation flips is reduced. For stations located close to this radiation node, taking into account both effects is thus crucial. For instance, based on the sole direct gravity effect, we would have expected the station AFI (IU network) to record almost zero signal during the 2018 $M_w = 8.2$ Fiji deep earthquake, while an accurate simulation of the overall PEGS almost predicts a 1.0 nm/s^2 downward acceleration. Finally, the overall PEGS radiation patterns of the two megathrust earthquakes differ both in shape and amplitude from their decomposed components. Indeed, while the direct and induced effects can be either positive or negative, the PEGS in the along-dip direction are expected to be negative for all epicentral distances, and to never

exceed 1.0 nm/s^2. To provide guidance for the search of elastogravity signals, the two effects must be computed.

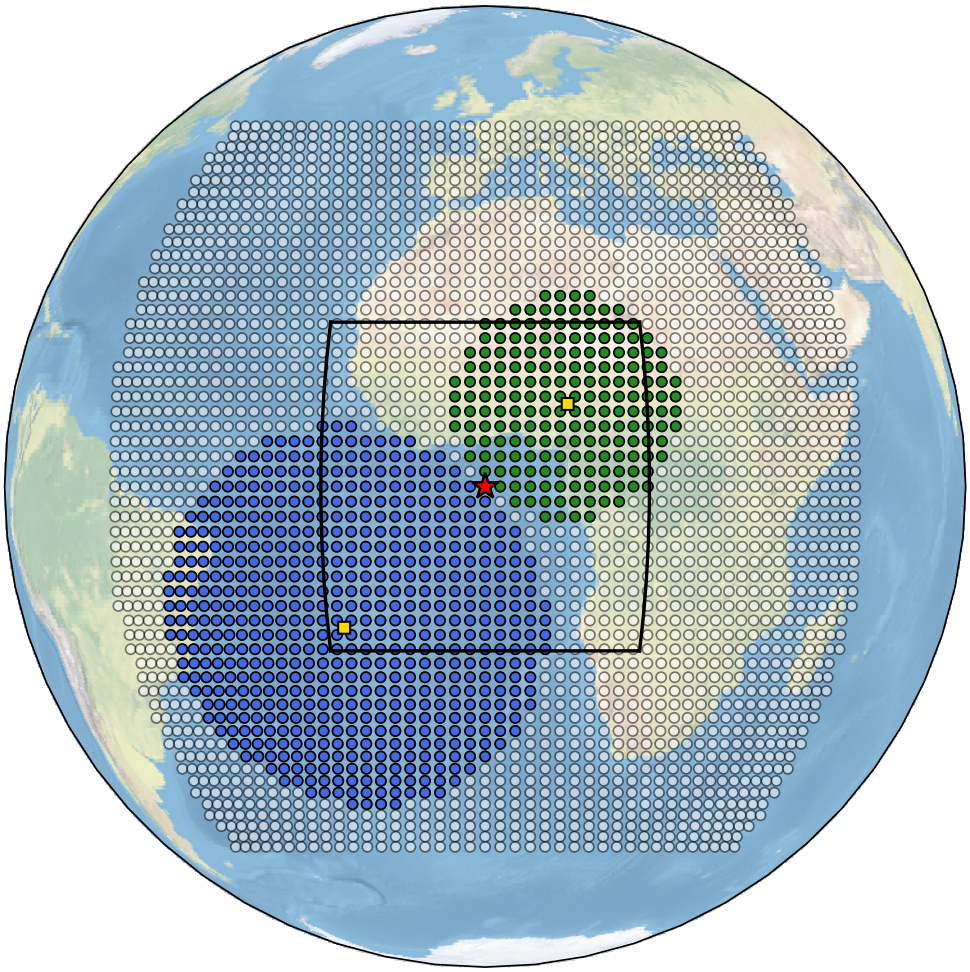

Figure S1. Grid used in the map computation of the gravity-induced elastic effect. The black lines represent the extent of the surface maps displayed in Figs. S2 to S5. The red star corresponds to the epicenter location, and the yellow squares to two locations where we compute the induced elastic effect $\ddot{\mathbf{u}}^{\mathbf{P}}$. The body forces $\rho\Delta\mathbf{g_k}$ induced by the earthquake are computed at each dot location, and in depth down to 4000 kilometers. Each of these dots excited by $\rho\Delta\mathbf{g_k}$ will then emit gravity-induced elastic waves in all directions. For the two square locations, the volume contributing to the induced elastic effect before P-wave arrival time is shown by the green and blue dots. The grid is centered at the (0°, 0°) location, and the sampling increased from 40 to 200 kilometers for plotting purposes.

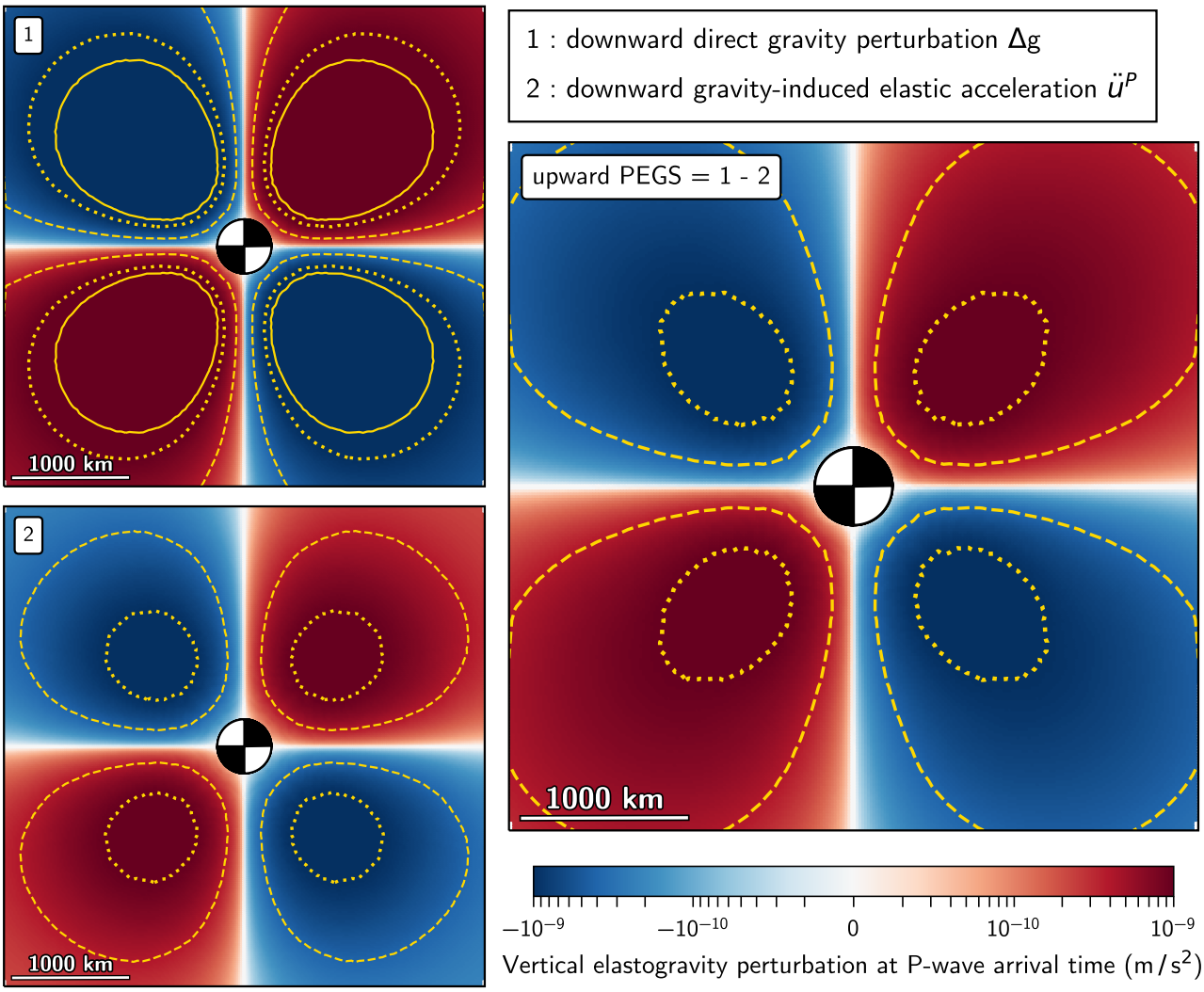

Figure S2. Expected vertical PEGS amplitudes at P-wave arrival time induced by a shallow strike-slip earthquake (strike = 0°, dip = 0°, rake = 90°, depth = 20 km) (right), decomposed into (top left) the direct gravity effect and (bottom left) the induced elastic effect. The earthquake epicenter location and focal mechanism is indicated by the beachball plot. Contour lines are for $\pm$ 0.4 $\times$ 10^{-9} m/s^{-2} (dashed), $\pm$ 1.0 $\times$ 10^{-9} m/s^{-2} (dotted) and $\pm$ 1.3 $\times$ 10^{-9} m/s^{-2} (solid).

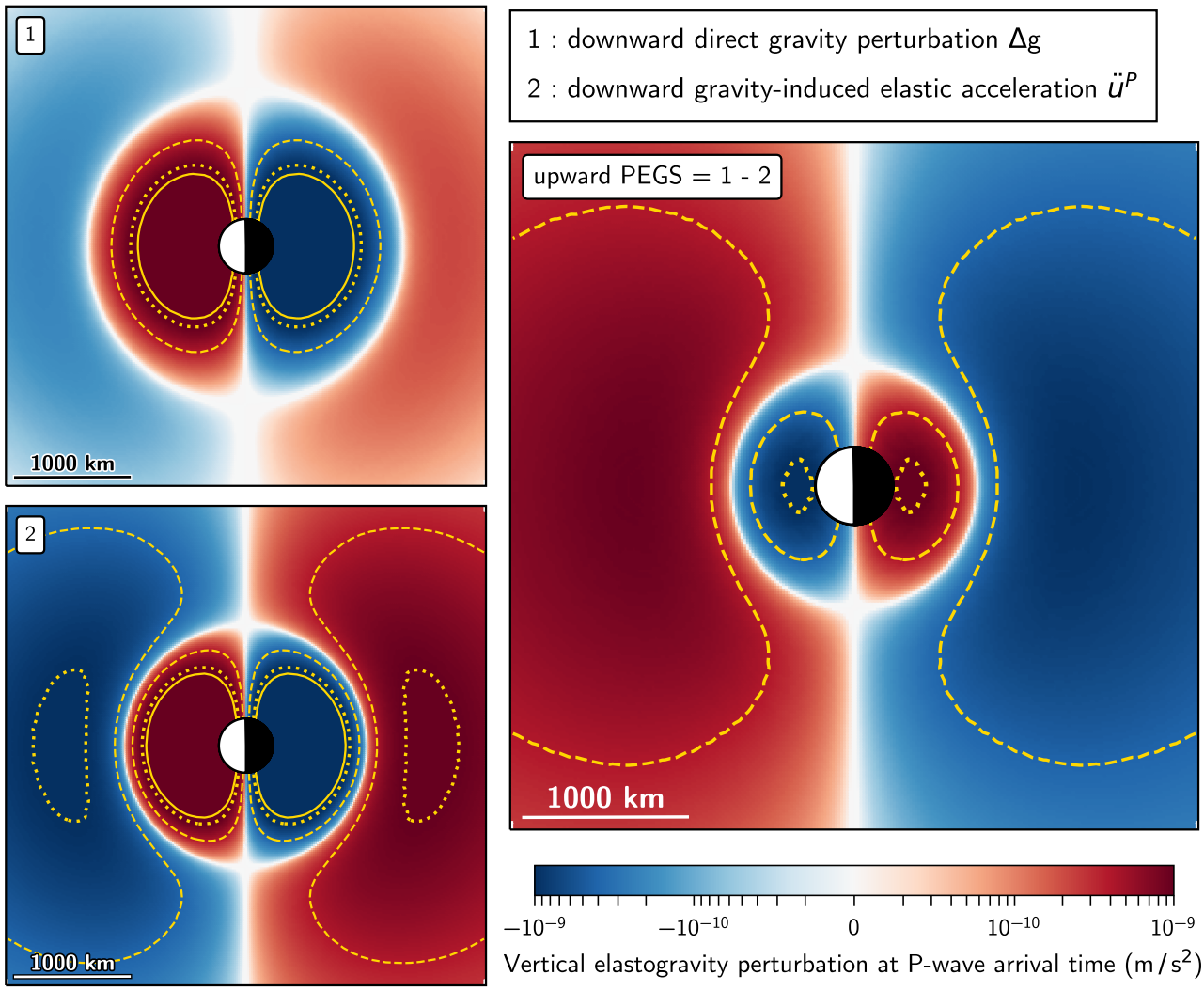

Figure S3. Expected vertical PEGS amplitudes at P-wave arrival time induced by a deep, dip-slip earthquake (strike = 0°, dip = 90°, rake = 0°, depth = 650 km) (right), decomposed into (top left) the direct gravity effect and (bottom left) the induced elastic effect. The earthquake epicenter location and focal mechanism is indicated by the beachball plot. Contour lines are for $\pm$ 0.4 $\times$ 10^{-9} m/s^{-2} (dashed), $\pm$ 1.0 $\times$ 10^{-9} m/s^{-2} (dotted) and $\pm$ 1.3 $\times$ 10^{-9} m/s^{-2} (solid).

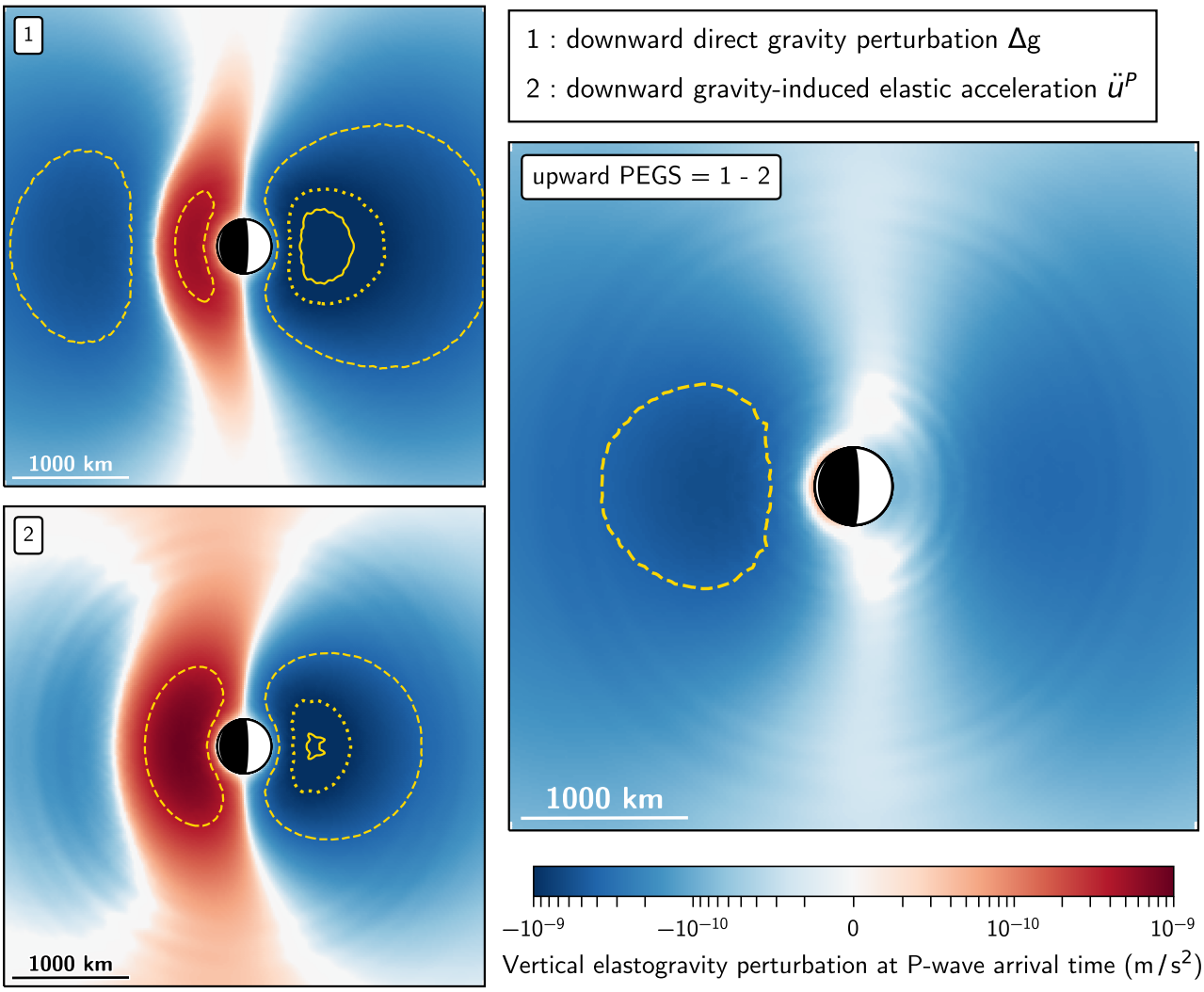

Figure S4. Expected vertical PEGS amplitudes at P-wave arrival time induced by a shallow dipping, megathrust earthquake (strike = 180°, dip = 10°, rake = 90°, depth = 20 km) (right), decomposed into (top left) the direct gravity effect and (bottom left) the induced elastic effect. The earthquake epicenter location and focal mechanism is indicated by the beachball plot. Contour lines are for $\pm$ 0.4 $\times$ 10^{-9} m/s^{-2} (dashed), $\pm$ 1.0 $\times$ 10^{-9} m/s^{-2} (dotted) and $\pm$ 1.3 $\times$ 10^{-9} m/s^{-2} (solid).

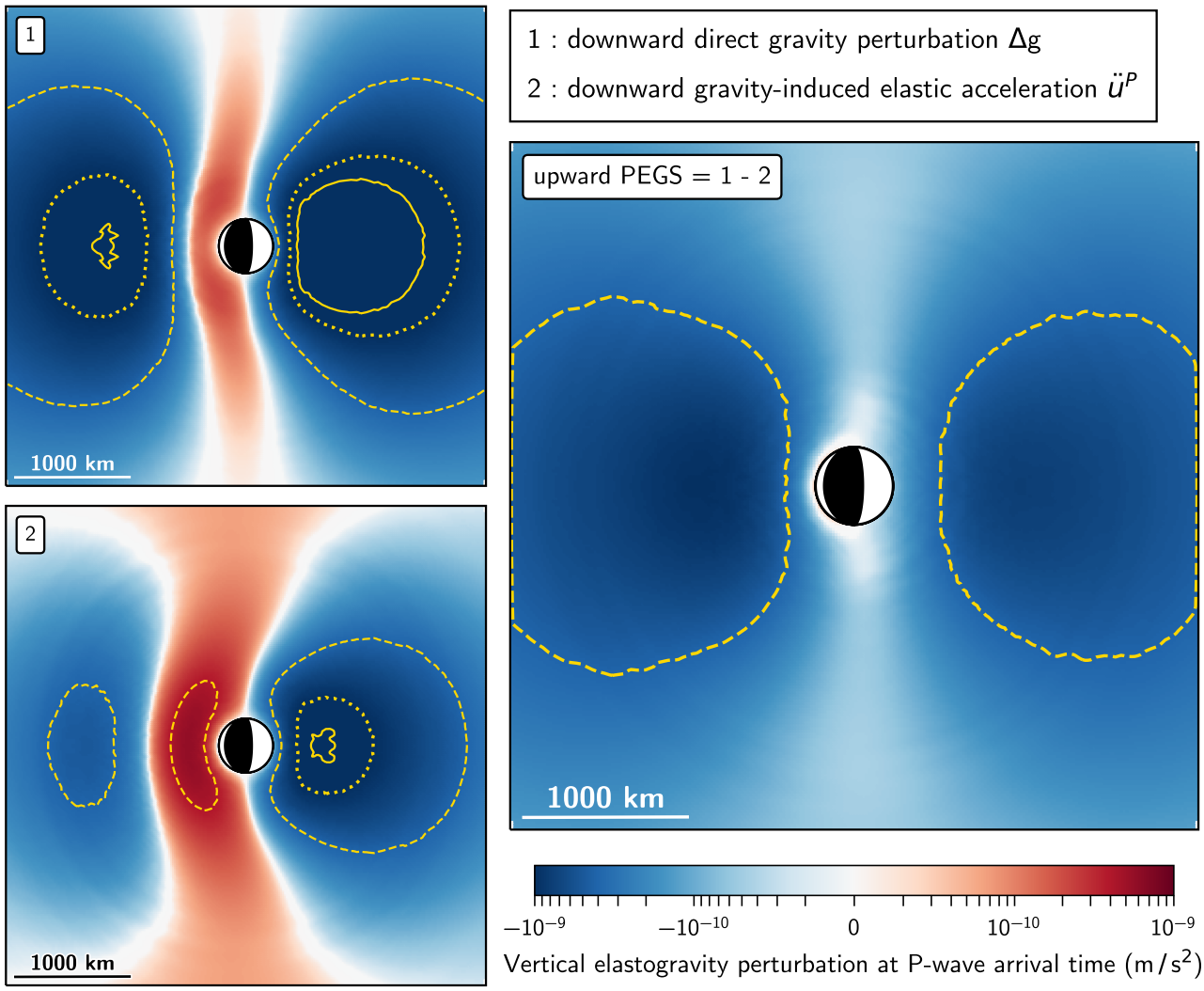

Figure S5. Expected vertical PEGS amplitudes at P-wave arrival time induced by a shallow dipping, megathrust earthquake (strike = 180°, dip = 20°, rake = 90°, depth = 20 km) (right), decomposed into (top left) the direct gravity effect and (bottom left) the induced elastic effect. The earthquake epicenter location and focal mechanism is indicated by the beachball plot. Contour lines are for $\pm$ 0.4 $\times$ 10^{-9} m/s^{-2} (dashed), $\pm$ 1.0 $\times$ 10^{-9} m/s^{-2} (dotted) and $\pm$ 1.3 $\times$ 10^{-9} m/s^{-2} (solid).

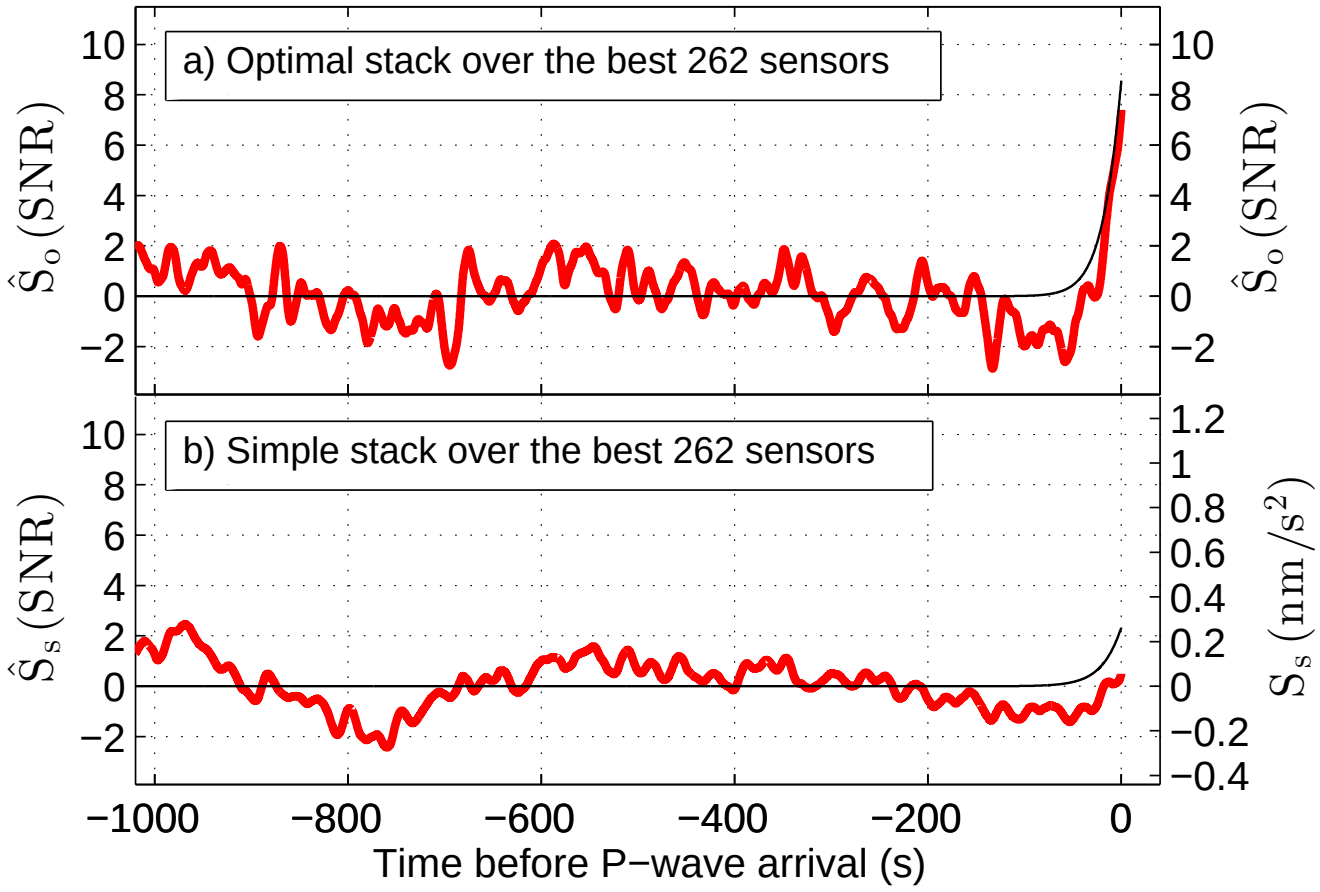

Figure S6. Same as Figure 7 from the main manuscript, but using all the 262 sensors. Note that in this case, PEGS are still clear with the optimal stack S_o^σ (SNR peaks to 7.4 compared to 10 in Figure 7), but cannot be detected any more with S_s^σ, due to the excessive number of stations with large noise σ_i.